Viscoelasticity of liquid water investigated using molecular dynamics simulations

Timothy J. O'Sullivan [1], Sridhar K. Kannam,[2] Debadi Chakraborty,[1]
Billy D. Todd [2,*] and John E. Sader [1,†]

[1]*ARC Centre of Excellence in Exciton Science, The University of Melbourne, Victoria 3010, Australia*
[2]*Department of Mathematics, Faculty of Science, Engineering and Technology,*
Swinburne University of Technology, Melbourne, Victoria 3122, Australia

Real liquids exhibit a viscoelastic response when excited mechanically to deform at sufficiently high frequency. We use classical nonequilibrium molecular dynamics simulations to calculate the linear viscoelastic response of extended simple point charge (SPC/E) water under both shear and elongation, for frequencies between 50 GHz and 10 THz and temperatures spanning the liquid phase of water at atmospheric pressure. These simulations are validated using equilibrium simulations that make use of Green-Kubo relations. Data up to and including 2 THz is fit to a single relaxation time linear Maxwell model, to facilitate comparison with reported experiments. We find that the resulting elastic moduli agree well with measurement, but this is not the case for the viscous moduli. This data also obeys a generalized Cauchy relation, implying that the elastic response of SPC/E water is dominated by central forces. This opens a pathway toward development of a simplified, molecular elastic water model for viscoelastic flows at high frequency. Furthermore, both elastic and loss moduli obey the time temperature superposition principle for frequencies up to 2 THz; an anomaly is observed above 2 THz, pointing to different physics. This behavior remains to be observed experimentally.

I. INTRODUCTION

A viscoelastic response occurs in any liquid, provided the liquid is stimulated mechanically to deform faster than it can relax to equilibrium. For complex liquids such as polymer melts and colloids, this relaxation process—and hence non-Newtonian behavior—is heavily dependent on the dynamics of their constituent particles (e.g., long polymer chains, colloid dispersed phase). The broad variety of particles used in complex liquids results in their characteristic relaxation times varying from microseconds to minutes.

Mechanical frequencies necessary to excite a viscoelastic response in a simple liquid such as water or glycerol are in the GHz to THz range. Consequently, experimental measurements of the viscoelastic response of simple liquids at room temperature and pressure have been limited until recently; these are discussed below. Piccirelli and Litovitz [1] used MHz ultrasonic techniques to show that glycerol exhibits a spectrum of relaxation times. This was achieved by using low-temperature measurements and extrapolating to higher temperature, assuming a linear variation. They found that the average shear and compression relaxation times for glycerol at $-18\,°C$ are 37 and 30 ns, respectively. Slie *et al.* [2] performed the same experiment on water-glycerol mixtures.

---

*btodd@swin.edu.au

†jsader@unimelb.edu.au

They observed that the relaxation times for all mixtures are in the pico- to nanosecond range. Furthermore, while it was not experimentally possible at the time to directly measure the same response in pure water, extrapolation of the results for water-glycerol mixtures suggested that the relaxation process for water occurs over a timescale of 1 picosecond.

More recently, inelastic Brillouin visible, x-ray, and ultraviolet scattering (BLS, IXS, UV) techniques have been used to directly probe the longitudinal dynamics of water and glycerol in the GHz and THz vibration regime. Using IXS, Cunsolo *et al.* [3] found that the longitudinal relaxation of water, assuming a simple Debye model of viscoelasticity, is again of order picoseconds. This relaxation displayed temperature-dependent Arrhenius behavior, which gives an activation energy very similar to that of the hydrogen bonding of water. This suggested that the longitudinal relaxation of water is due to local structure rearrangements induced by hydrogen bonding. Monaco *et al.* [4] repeated these IXS experiments, the data analysis of which involved a more sophisticated approach, involving density fluctuations, the structure factor of water, and the memory function—as opposed to the previous simple assumption of a Debye model. As a result, they calculated the temperature dependence of the compliance relaxation time. Using UV, Masciovecchio *et al.* [5] found again that the structural relaxation of water is of order picoseconds, the temperature-dependent behavior of which was in excellent agreement with mode coupling theory (MCT). This suggested that the glass-transition for supercooled water occurs at 220 K. Giugni and Cunsolo [6] later utilized BLS, UV and IXS in a joint study of the structural dynamics of glycerol. The use of three different scattering techniques and incorporation of previous studies using ultrasound (US) [7,8] provided a comprehensive dataset for the temperature and frequency dependence of glycerol's sound speed. This dataset was well approximated by a Cole-Davidson (CD) [9] profile yet was poorly approximated using a Debye model. It was observed that the mean compliance time of glycerol varied from 1–100 picoseconds. More recently, time-domain Brillouin scattering (TDBS) has been used to directly probe the shear dynamics of glycerol and various other liquids. Klieber *et al.* [10] utilized TDBS to measure the temperature and frequency dependence of the shear and longitudinal modulus of glycerol and found that a generalized Cauchy relation was obeyed. Currently, there are no direct experimental measurements of the shear relaxation process of water.

The vibration modes of metallic nanoparticles have been investigated extensively using ultrafast laser techniques. The size of these particles ensures the period of their acoustic vibration is in the above-mentioned pico- to nanosecond regime–with vibrational frequencies in the GHz to THz range. When these particles are immersed in simple (nominally Newtonian) liquids, such as water or glycerol, they can in principle interrogate the natural relaxation processes of these liquids. Specifically, the shear relaxation process is interrogated by the extensional modes of the particles, while the longitudinal relaxation process is interrogated by the breathing modes. This has been demonstrated in a series of recent experiments, which we now discuss.

Pelton *et al.* [11] observed a significant deviation from Newtonian theory for vibrating gold nanoparticles immersed in mixtures of water and glycerol. The response was well described by a linear Maxwell model, with no fitting parameters. Similarly, Yu *et al.* [12] observed that the vibrational lifetimes of gold nanowires immersed in glycerol and ethylene-glycol are enhanced relative to Newtonian model calculations. A general theory for compressible viscoelastic flows was used to interpret these measurements, where good agreement was again observed with no fitting parameters based on the viscoelastic experimental dataset of Slie *et al.* [2]. While these results highlight the potential for direct measurement of the viscoelastic response of simple liquids, they are also of significance to the burgeoning field of nanomechanical and nanoelectromechanical systems (NEMS). As the miniaturization of NEMS devices continues, the frequencies that they use increases. In biological settings, for example, the resonant frequencies of some of these devices may be high enough to excite a viscoelastic response in the surrounding water environment; platinum particles have been observed to resonate in the THz range [13]. Therefore, knowledge of the viscoelasticity of prevalent simple liquids, such as water and water mixtures, is expected to hold greater significance for the design and operation of future NEMS devices.

The viscoelastic properties and relaxation times of any liquid arise from its molecular interactions and their associated timescales. Classical molecular dynamics (MD) simulations can model these interactions over arbitrarily small timescales. Subsequently, MD simulations, combined with accurate molecular force-fields, are an effective tool in determining the real (storage, elastic) and imaginary (loss, viscous) shear and elongational viscoelastic (mechanical) moduli of liquids. The mechanical moduli of complex liquids such as polymer solutions and melts have been extensively characterized using MD simulations [14–16]. Similar MD simulations have also been used to investigate the mechanical moduli and nonlinear viscoelasticity of n-hexadecane liquids [17,18].

Turning to simple liquids, Rahman and Stillinger [19] studied the propagation of sound waves in water via equilibrium MD simulations. They observed two peaks in the density fluctuations of their water model, consistent with a "slow" and "fast" sound speed. This transition from slow to fast sound speed was later observed in the scattering experiments mentioned previously [3–5]. The strong temperature dependence of this transition implied the underlying mechanism was dynamic, i.e., liquid water was displaying a viscoelastic response. While studying viscoelasticity was not the primary motive of that study, Rahman and Stillinger [19] had presented the first investigation of the viscoelastic response of water via classical MD simulations. Sciortino and Sastry [20] and Balucani *et al.* [21] followed by directly investigating this transition from slow to fast sound using MD simulations. The data reported was satisfactorily explained with a linear Maxwell model. Furthermore, the relaxation times in these studies were later found to be in good agreement with experiment [3].

While these previous (equilibrium) MD studies have been successful in simulating one aspect of the viscoelasticity of water, there are several outstanding facets. First, these studies monitored the density fluctuations of water from which the longitudinal elastic (storage) modulus was calculated—all other moduli were ignored. An alternate approach to calculate the frequency dependent viscoelastic behavior is to use equilibrium MD simulations coupled to a Green-Kubo [22–24] analysis of the stress time series. More recently, Lacevic and Sader [25] extended a nonequilibrium MD (NEMD) technique—commonly used to study the viscoelasticity of complex liquids—and performed MD simulations to characterize the mechanical moduli of the simple liquid, glycerol. This showed good agreement with the long-standing measurements of Litovitz and coworkers. In contrast with the above-mentioned equilibrium MD studies of water, this nonequilibrium approach was able to characterize the elastic and viscous moduli under both shear and elongation.

In this study, we utilize this characteristic feature of nonequilibrium MD to simulate the complete viscoelastic response of water under both shear and elongation. This is performed for frequencies ranging from 50 GHz and 10 THz, temperatures across the liquid phase of water and at atmospheric pressure. To validate this dataset, we also perform equilibrium MD simulations that makes use of Green-Kubo relations [22–24], where excellent agreement is observed. This comparison also shows that the behavior of the extended simple point charge (SPC/E) model for water exhibits an anomolous viscoelastic response above 2 THz that is not well described by a single relaxation time Maxwell model. We also present data for the flexible bond point charge SPC/Fw model [26], which gives identical results to the SPC/E model. Our study provides an important dataset for comparison with future measurements that may seek to probe or utilize the viscoelastic response of water, and for the further development of molecular models for water that focus on viscoelasticity.

We begin with a brief discussion of the molecular model and simulation approach used in this study. The simulation techniques used to characterize the mechanical moduli of water are then presented. Following a discourse summarizing the raw viscoelastic data calculated from the simulations, we draw comparisons with the linear Maxwell model determined from experimental measurements of the shear and bulk viscosities [27,28] and the predicted high frequency moduli of water [2]. We then fit a linear Maxwell model to the present data up to and including 2 THz, which allows derivation of an empirical formula for the temperature dependent shear and compressional relaxation times of this water model, assuming a single relaxation process. Finally, we investigate the emergence of a generalized Cauchy relation for this water model, explore the applicability of the time temperature superposition principle and discuss potential consequences.
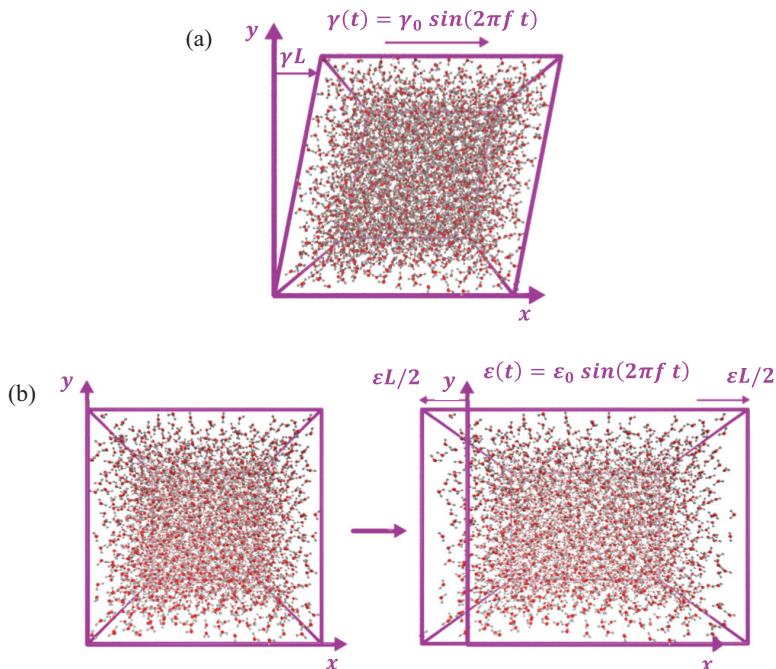
FIG. 1. Schematic of shear (a) and elongational (b) deformations applied to the simulation box in this study. Note that the size of the deformation in each figure is exaggerated for visual purposes only.

II. WATER MODEL AND SIMULATION DETAILS

In this section, we provide details of the MD simulations used to probe the viscoelastic properties of water. This is achieved using the SPC/E model of Berendsen [29], which reproduces the temperature dependent density and diffusion coefficient of water at standard conditions. Model details are found in the work of Wu *et al.* [26]. We prepare the simulation samples by replicating 3425 SPC/E water molecules in a $4.8 \times 4.8 \times 4.8$ nm^3 cubic domain using the software package Packmol [30]. This sample then serves to produce five equilibrium samples for twelve temperatures in the range 0–100 °C, at atmospheric pressure. This is achieved with LAMMPS software [31] by completing 3 ns duration, 1 fs timestep simulations with periodic boundary conditions. These simulations require a Nosé-Hoover style thermostat-barostat [32–34] with respective damping parameters 100 and 1000, to ensure that the desired temperature and pressure are achieved. With a sufficient number of equilibrium SPC/E water samples prepared, we now determine the strain-amplitudes γ_0 and ε_0. The simulation method detailed by Lacevic and Sader [25] is then applied to probe the shear and longitudinal moduli of water. We proceed with an overview of this method and a description of the reason that this method enables the viscoelastic response to be probed.

The boundaries of the above-mentioned equilibrium samples are changed from orthogonal to triclinic, allowing the geometry of the boundary to be deformed. The following shear and longitudinal strains are then applied separately in the *x*-direction of the simulation box:

$$\gamma(t) = \gamma_0 \sin(2\pi f t), \quad \varepsilon(t) = \varepsilon_0 \sin(2\pi f t), \tag{1}$$

where f is the frequency, γ is the shear-strain with amplitude γ_0 and ε is the longitudinal-strain with amplitude ε_0. These strains are shown schematically in Figs. 1(a) and 1(b).

To ensure the water molecule dynamics obey Newton's equations of motion, the strains are coupled to the atoms via the so-called "atomic" SLLOD equations of motion [35–38], which are implemented in LAMMPS:

$$\dot{\mathbf{r}}_{i,\alpha} = \frac{\mathbf{p}_{i,\alpha}}{m_{i,\alpha}} + \mathbf{r}_{i,\alpha} \cdot \nabla \mathbf{u}, \tag{2}$$

$$\dot{\mathbf{p}}_{i,\alpha} = \mathbf{F}_{i,\alpha} - \mathbf{p}_{i,\alpha} \cdot \nabla \mathbf{u} - \zeta \mathbf{p}_{i,\alpha}, \tag{3}$$

where i represents molecule i and α represents the atomic site α. Thus, $m_{i,\alpha}$, $\mathbf{r}_{i,\alpha}$ and $\mathbf{p}_{i,\alpha}$ are the mass, position and thermal momentum of the atomic site α of molecule i, $\mathbf{F}_{i,\alpha}$ is the total force on the atomic site α of molecule i due to interatomic, bond and angle forces, ζ is the Nosé-Hoover thermostat multiplier and $\mathbf{u}$ is the velocity field. It has been suggested [39,40] that LAMMPS implements p-SLLOD [41] or equivalently g-SLLOD [39,40,42], but this is not the case [43]. The deficiencies of p-SLLOD have been discussed elsewhere [36,37].

For a shear deformation we have

$$\nabla \mathbf{u} = \dot{\gamma}(t)\hat{x}\hat{y}, \tag{4}$$

and for longitudinal deformation

$$\nabla \mathbf{u} = \dot{\varepsilon}(t)\hat{x}\hat{x}. \tag{5}$$

These strain simulations are performed on each equilibrium sample for frequencies in the range 50 GHz–10 THz. The simulation duration is chosen to achieve sufficient signal-to-noise given available computational resources; see Appendix A.

Throughout these simulations we compute the atomic stress tensor every five time-steps using

$$\boldsymbol{\sigma}(t) = -\mathbf{P}(t), \tag{6}$$

where $\mathbf{P}$ is the atomic pressure tensor as implemented by LAMMPS, which is given by

$$\mathbf{P}(t) = \frac{1}{V}\left(\sum_{i=1}^{N_m}\sum_{\alpha=1}^{N_{s,i}} m_{i,\alpha}\mathbf{c}_{i,\alpha}\mathbf{c}_{i,\alpha} - \frac{1}{2}\sum_{i=1}^{N_m}\sum_{\alpha=1}^{N_{s,i}}\sum_{j=1}^{N_m^*}\sum_{\beta=1}^{N_{s,j}^*} \mathbf{r}_{i,\alpha,j,\beta}\mathbf{F}_{i,\alpha,j,\beta}\right), \tag{7}$$

where N_m is the number of molecules and $N_{s,i}$ is the number of atomic sites of molecule i. Here, $\mathbf{c}_{i,\alpha}$ is the peculiar velocity (inertial reference frame velocity minus the streaming velocity) of the atomic site α of molecule i, $\mathbf{r}_{i,\alpha,j,\beta}$ is the position of the atomic site α of molecule i, relative to the atomic site β of molecule j, $\mathbf{F}_{i,\alpha,j,\beta}$ is the force on atomic site α of molecule i due to the atomic site β of molecule j, and V is the volume of the system. N_m^* and $N_{s,j}^*$ indicate that the summation must also include periodic images. Justification for use of the atomic pressure tensor and atomic SLLOD is provided in Appendix B.

These strain simulations allow interrogation of the viscoelasticity of water because a linear viscoelastic system exhibits the following stress responses under strains specified in Eq. (1):

$$\sigma_{xy}(t) = \sigma_0 \sin(2\pi f t + \delta_s), \quad \sigma_{xx}(t) = \sigma_0' \sin(2\pi f t + \delta_e), \tag{8}$$

for shear and compression, respectively. We calculate $\sigma_0, \sigma_0', \delta_s,$ and δ_e by applying a discrete Fourier transform (DFT) to the xy and xx components of the atomic stress tensor time-series. The real and imaginary parts of the shear and longitudinal moduli, G and M, are then calculated for each
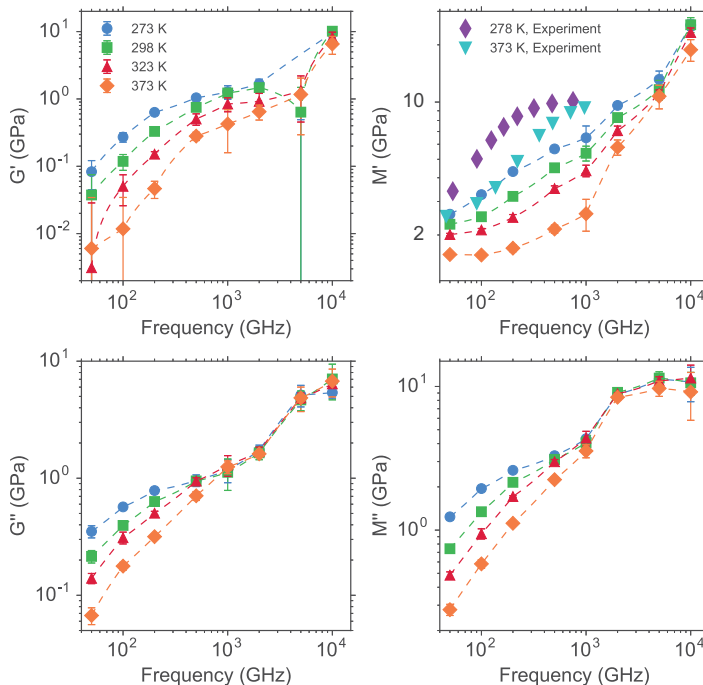
FIG. 2. Viscoelastic data versus frequency obtained using the SPC/E model of water for the storage and loss moduli for shear and elongation, using a temperature of $T = 273$ K (blue circles), 298 K (green squares), 323 K (red triangles), 373 K (orange diamonds). Each data point represents the mean of five simulations and error bars are one standard deviation. Experimental data [3] is given for M' at $T = 278$ K (purple diamonds) and 373 K (cyan upside-down triangles). Interpolating lines are provided between the simulation data points to guide the eye.

frequency and temperature via the following equations:

$$G' = \frac{\sigma_0}{\gamma_0} \cos \delta_s, \quad G'' = \frac{\sigma_0}{\gamma_0} \sin \delta_s, \quad M' = \frac{\sigma_0'}{\varepsilon_0} \cos \delta_e, \quad M'' = \frac{\sigma_0'}{\varepsilon_0} \sin \delta_e. \tag{9}$$

III. RESULTS

Figure 2 gives numerical results for the storage and loss components of the shear and longitudinal moduli, where a subset of temperatures investigated are shown for visual clarity. The subfigure in Fig. 2 for the longitudinal storage modulus, M', also includes a comparison with available experiments [3], where the SPC/E model clearly underestimates M' by up to a factor of 4; this aspect is discussed below. The full viscoelastic numerical dataset is provided in the Appendix C.

All moduli are observed to increase with temperature for frequencies less than or equal to 2 THz; this temperature trend does not hold for higher frequencies. Furthermore, the associated simulation error (indicated by the error bars in Fig. 2) for frequencies of 5 THz and above increase strongly and the observed monotonicity in the shear moduli is broken. Since this anomaly occurs at high-frequency and a profile-biased Nosé-Hoover thermostat is used, this observation would seem to suggest that a transition to the *string phase* of the liquid [35] has occurred. However, analysis of the oxygen-oxygen pair distribution function reported in Appendix D shows that the system undergoes no structural change as frequency increases, thus no transition to the string phase occurs.

To confirm that the observed anomalous behavior beyond 2 THz is not due to an unknown NEMD simulation artefact, 20 ns equilibrium simulations of SPC/E water are performed for a range
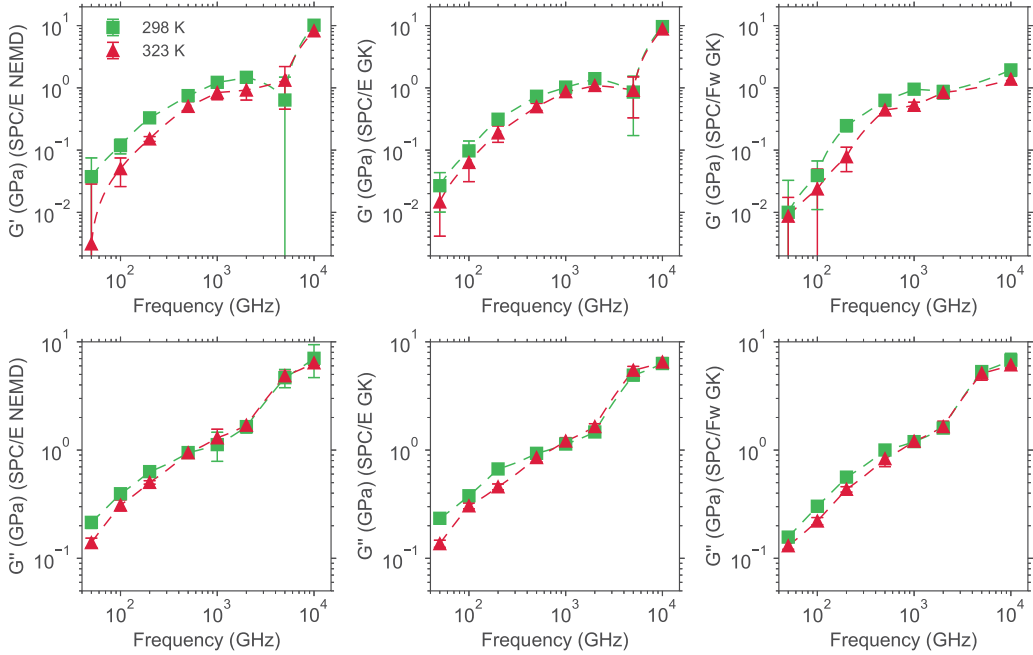
FIG. 3. Comparison of shear viscoelastic moduli versus frequency using the SPC/E and SPC/Fw models at a temperature $T = 298\,\text{K}$ (green squares) and 323 K (red triangles). The first column shows the NEMD simulation data from Fig. 2, the second and third columns give data from equilibrium Green-Kubo simulations of the SPC/E and SPC/Fw models, respectively. Each data point is the mean of five simulations and error bars are one standard deviation. Interpolating lines are provided between the simulation data points to guide the eye. Note that the storage modulus for SPC/Fw at 5 THz is negative and has been omitted for visual clarity.

of temperatures; components of the stress tensor are sampled every 5 fs. The Green-Kubo (GK) [22–24] relations are then used to calculate the storage and loss components of the shear modulus, which are, respectively, given by

$$G'(\omega) = \frac{T}{5k_\text{B}V} \int_0^\infty \omega \sin(\omega t) \sum_i \langle \sigma_i(t)\sigma_i(0)\rangle dt, \qquad (10)$$

$$G''(\omega) = \frac{T}{5k_\text{B}V} \int_0^\infty \omega \cos(\omega t) \sum_i \langle \sigma_i(t)\sigma_i(0)\rangle dt, \qquad (11)$$

where σ is the stress tensor and summation is over all five components of the symmetric traceless stress tensor, i.e., σ_{xy}, σ_{xz}, σ_{yz}, $(\sigma_{xx} - \sigma_{yy})/2$ and $(\sigma_{yy} - \sigma_{zz})/2$, T is temperature, V is the system volume and k_B is Boltzmann's constant. The first and second columns of Fig. 3 show the NEMD shear modulus and (alternate) equilibrium simulations, respectively. These two sets of results are identical to within simulation error. This confirms that the anomalous behavior beyond 2 THz is not an artefact of the NEMD simulation scheme, but is intrinsic to the SPC/E model.

To examine if the anomalous behavior above 2 THz is due to the rigid-bonds of the SPC/E model, the above equilibrium GK simulations are repeated using the flexible bond simple point charge (SPC/Fw) model [26]. This data is given in the third column of Fig. 3. The SPC/Fw simulation data closely resemble the SPC/E results, again with anomalous behavior above 2 THz. SPC/Fw results for the loss moduli, G'', closely match those for SPC/E over the entire frequency range, but some differences occur in the storage moduli, G', above 2 THz. Even so, the observed anomalous

behavior above 2 THz cannot be explained by relaxation of the rigid bonds of the SPC/E model. The remainder of this article focuses on the SPC/E model.

The above simulations show that the viscoelastic response above 2 THz cannot be described by a linear (single relaxation time) Maxwell model. Thus, the following analysis only includes viscoelastic data up to 2 THz. The origin of the anomalous behavior above 2 THz is explored further below.

A. Comparison with measurement

Experiments in Refs. [2] are reported in terms of parameters in a linear Maxwell model,

$$G'(\omega) = \frac{G_\infty (\omega \lambda_{\mathrm{sh}})^2}{1 + (\omega \lambda_{\mathrm{sh}})^2}, \tag{12a}$$

$$G''(\omega) = \frac{G_\infty (\omega \lambda_{\mathrm{sh}})}{1 + (\omega \lambda_{\mathrm{sh}})^2}, \tag{12b}$$

$$M'(\omega) = K_0 + \frac{K_2 (\omega \lambda_{\mathrm{comp}})^2}{1 + (\omega \lambda_{\mathrm{comp}})^2} + \frac{4}{3} \frac{G_\infty (\omega \lambda_{\mathrm{sh}})^2}{1 + (\omega \lambda_{\mathrm{sh}})^2}, \tag{12c}$$

$$M''(\omega) = \frac{K_2 (\omega \lambda_{\mathrm{comp}})}{1 + (\omega \lambda_{\mathrm{comp}})^2} + \frac{4}{3} \frac{G_\infty (\omega \lambda_{\mathrm{sh}})}{1 + (\omega \lambda_{\mathrm{sh}})^2}, \tag{12d}$$

that are fit to the measured data. Here, $\omega = 2\pi f$ is the angular frequency, λ_{sh} and λ_{comp} are the shear and compression relaxation times, respectively, $G_\infty = \mu/\lambda_{\mathrm{sh}}$ is the high-frequency shear modulus, μ is the shear viscosity, and $K_2 = \mu_{\mathrm{B}}/\lambda_{\mathrm{comp}}$ is the difference of the limiting high and low frequency bulk moduli, i.e., $K_2 = K_\infty - K_0$ where μ_{B} is the bulk viscosity. The high-frequency longitudinal modulus is

$$M_\infty = K_\infty + \tfrac{4}{3} G_\infty. \tag{13}$$

Note that all longitudinal moduli, M', M'' and M_∞, are related to their respective shear and bulk moduli in an identical manner.

Figures 4 and 5 show a comparison between the raw simulation data of the present study and that of a linear Maxwell model based on experiment [2,3,27,28]. We discuss the results for the shear and longitudinal moduli separately.

1. Shear modulus

From Fig. 4 it is evident that linear Maxwell model predictions [2] (derived from experimental data) for the storage modulus, G', agree with SPC/E model simulations over the temperature range studied: A monotonic increase in modulus with frequency is observed that plateaus somewhat at high frequency. While some discrepancy creeps in at higher temperature, overall the agreement is reasonable. The same is not true for the loss modulus, G'', where good agreement is achieved only for lower frequency. This shows that the MD linear viscoelastic behavior is not well represented by a Maxwell model with a single relaxation time, as was noted in Ref. [2] for experimental data on water.

2. Longitudinal modulus

Only temperatures up to and including 323 K are considered in Fig. 5 due to limited experimental data for the bulk viscosity. As for the shear modulus discussed above, the linear Maxwell model fits to experimental data align with SPC/E model simulation data for the longitudinal storage component, M', though no plateau at high frequency is observed in the simulation data. Interestingly, the increase in modulus in the SPC/E model begins at higher frequency relative to experiment.
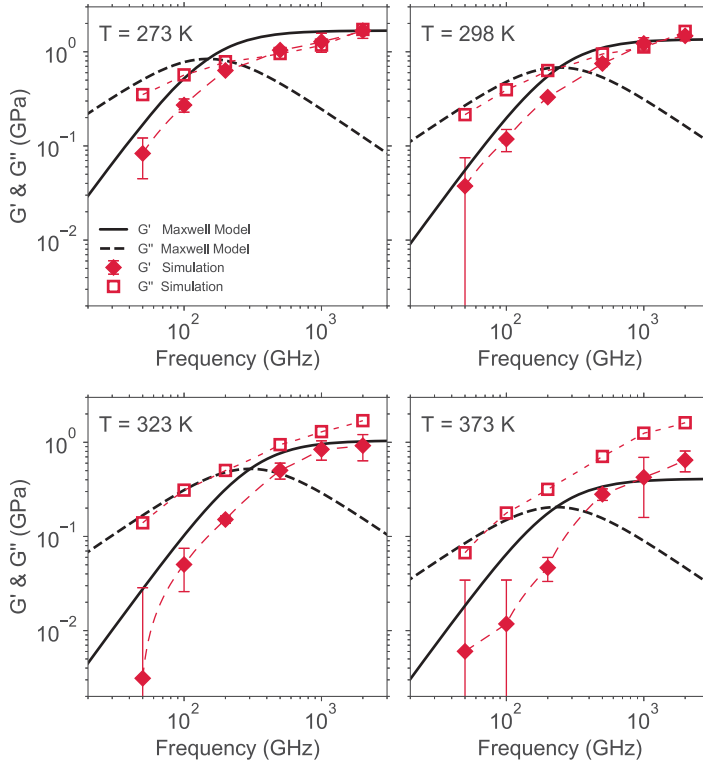
FIG. 4. Shear modulus (storage and loss) for water as a function of frequency. The four subfigures give results for temperatures of $T = 273, 298, 323, 373$ K. Experimental data (black curves) are provided by single relaxation time Maxwell model fits of Refs. [2,27]. Interpolating lines (dashed red) are provided between the simulation data points.

B. High-frequency moduli and relaxation times

Reference [2] provides data for the high-frequency moduli G_∞ and M_∞ of water. Since frequencies above 2 THz are not considered for this single relaxation time linear Maxwell model analysis, we compare simulation values for G' and M' at 2 THz to the high-frequency moduli obtained experimentally. Separate linear fits to the simulation data for G_∞ and M_∞ at 2 THz, as a function of temperature (K), give

$$G_\infty > G_{2\,\mathrm{THz}} \approx (4.55 \pm 0.489) + (-0.0107 \pm 0.00858)T, \tag{14a}$$

$$M_\infty > M_{2\,\mathrm{THz}} \approx (18.9 \pm 0.228) + (-0.0351 \pm 0.00399)T. \tag{14b}$$

Figure 6 shows a comparison between Eqs. (14a) and (14b) and experimental data [2]. The high-frequency shear modulus approximation, $G_\infty \approx G_{2\,\mathrm{THz}}$, derived from simulations of the SPC/E model is in excellent agreement with experimental data for G_∞. In contrast, the high-frequency longitudinal modulus approximation, $M_\infty \approx M_{2\,\mathrm{THz}}$, overestimates experiment (red dashed curve) by at most 20%. The good agreement between simulation and experiment for shear are in contrast to the elongation data. This is directly related to the capacity of the SPC/E model to accurately predict the shear viscosity but not the bulk viscosity of water where a strong underestimate is observed, see below. The same microscopic mechanisms driving this underestimate in the bulk viscosity contribute to high-frequency elongation processes, consistent with the results presented in Fig. 6.

Reference [2] also provides experimentally derived results for the shear and compressional relaxation times of water, which when expressed in terms of a single relaxation time Maxwell model
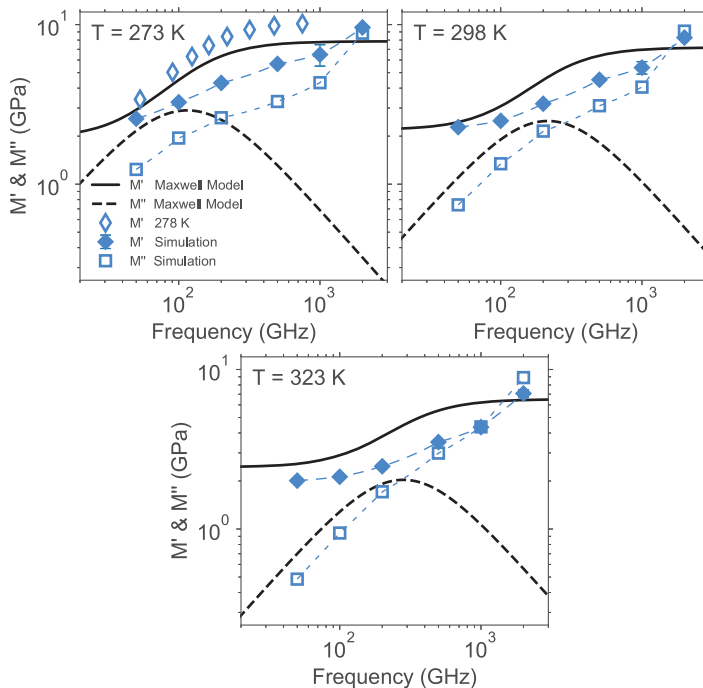
FIG. 5. Longitudinal modulus (storage and loss) for water as a function of frequency. The three subfigures give results for temperatures of $T = 273, 298, 323$ K. Experimental data (black curves) are provided by the single relaxation time Maxwell model fits of Refs. [2,28]. Experimental data [3] for M' at $T = 278$ K is also shown. Interpolating lines (dashed blue) are provided between the simulation data points.

gives

$$\lambda_{\text{sh}} = \frac{\mu}{G_\infty}, \quad \lambda_{\text{comp}} = \frac{\mu_{\text{B}}}{K_2}. \tag{15}$$

Equations (14a), (14b), and (15) are used with MD simulation results for the bulk and shear viscosities of the SPC/E model [44] to calculate the corresponding temperature-dependent shear
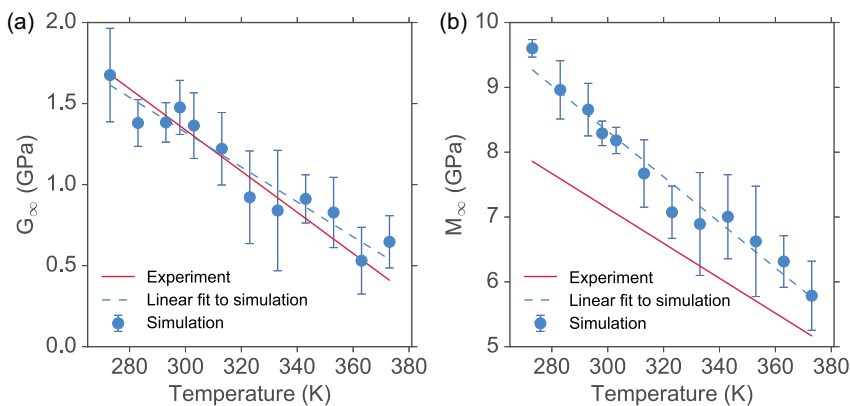
FIG. 6. High-frequency viscoelastic moduli of water. (a) Shear modulus with Eq. (14a) (dashed blue line), and (b) longitudinal modulus with Eq. (14b) (dashed blue line), versus temperature. Experiment (solid red curves) and simulation data (dots with error bars). The dashed blue lines, defined in Eqs. (14a) and (14b), are obtained from separate linear regressions of the simulation data for G_∞ and M_∞, respectively.
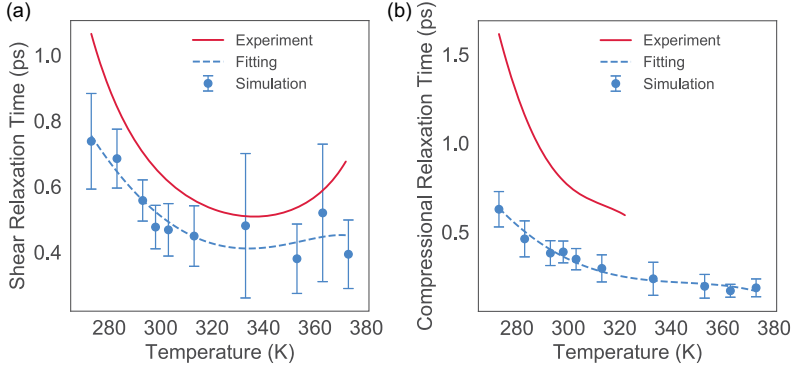
FIG. 7. Comparison of relaxation times for water as a function of temperature. (a) Shear relaxation time, λ_{sh}, and (b) compressional relaxation time, λ_{comp}, derived from a single relaxation time Maxwell model. Experimental results for (a) shear [2,27], and (b) compression [2,28] are the red curves, whereas data for SPC/E water are the dots with error bars; the blue curves are best fits.

and compression relaxation times. A cubic polynomial interpolation of the shear and bulk viscosity data reported in Ref. [44] is used, motivated by previous work [28]. Performing this fit gives the following formulas (mPa s),

$$\mu \approx a_0 + a_1 T + a_2 T^2 + a_3 T^3, \tag{16}$$

$$\mu_B \approx b_0 + b_1 T + b_2 T^2 + b_3 T^3, \tag{17}$$

where

$$
\begin{aligned}
a_0 &= 59.3, & b_0 &= 186, \\
a_1 &= -0.497, & b_1 &= -1.59, \\
a_2 &= 1.42 \times 10^{-3}, & b_2 &= 4.57 \times 10^{-3}, \\
a_3 &= -1.34 \times 10^{-6}, & b_3 &= -4.40 \times 10^{-6},
\end{aligned}
$$

with coefficients of determination being $R^2 = 0.9979$ and 0.9955 for μ and μ_B, respectively. Combining Eqs. (14a), (14b), (16), and (17) gives the following empirical formulas for the shear and compressional relaxation times for the SPC/E model (ps):

$$\lambda_{sh} \approx \frac{a_0 + a_1 T + a_2 T^2 + a_3 T^3}{4.55 - 0.0107T}, \tag{18a}$$

$$\lambda_{comp} \approx \frac{b_0 + b_1 T + b_2 T^2 + b_3 T^3}{4.64 - 0.0116T}, \tag{18b}$$

where a linear fit for K_0 is used to calculate the functional form of K_2.

Figure 7 presents a comparison between the simulated relaxation times in Eqs. (18a) and (18b) and those of experiment [2]. We remind the reader that these relaxation times are derived from a single relaxation time linear Maxwell model, which facilitates comparison to experimental data in Ref. [2]. The shear and longitudinal results are now discussed.

1. Shear relaxation time

Simulation data as described by Eq. (18a) are observed to predict experiments for λ_{sh} with good accuracy ($\approx 20\%$ underestimate) and the temperature at which a minimum occurs is accurately recovered. Because Eq. (14a) for G_∞ agrees well with experiment, the observed difference in
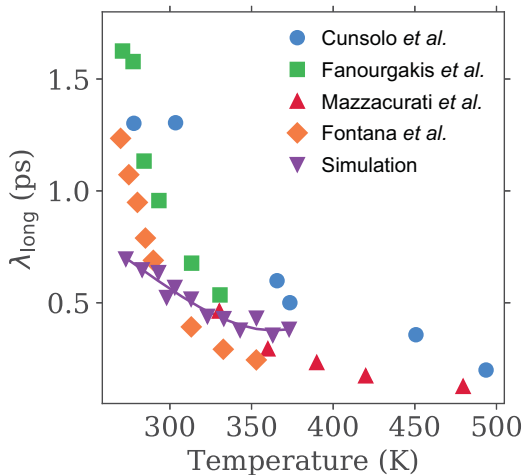
FIG. 8. Longitudinal relaxation time, λ_{long}, versus temperature. Comparison of experimental data by Cunsolo *et al.* [3], Fanourgakis *et al.* [44], Mazzacurati *et al.* [45], and Fontana *et al.* [46] with present simulation data. It is observed that simulation data for the SPC/E model of water (purple upside-down triangles) are of comparable magnitude to those previously obtained from experiments but display a weaker variation with temperature. The purple curve is a best fit to the simulation data.

λ_{sh} must be due to the shear viscosity of the SPC/E model. It is known that this shear viscosity underestimates experiment by up to 30% [28], which is consistent with Fig. 7(a).

2. Compressional relaxation time

Simulations described by Eq. (18b) exhibit a decrease in the compressional relaxation time, λ_{comp}, with increasing temperature that also qualitatively agrees with measurement. However, the discrepancy is larger than that observed for the shear relaxation time, cf. Figs. 7(a) and 7(b). Importantly, the SPC/E model is known to underestimate the bulk viscosity of water by at least 50% [28] while the simulated modulus $M_\infty \approx M'_{2\,\text{THz}}$ in Eq. (14b) overestimates experiment (discussed above). These combined effects explain the underestimate by Eq. (18b) observed in Fig. 7(b).

Longitudinal relaxation times, λ_{long}, can be determined by fitting a Debye model,

$$M' = M_\infty + \frac{M_0 - M_\infty}{1 + (\omega \lambda_{\text{long}})^2}, \tag{19}$$

to simulation data for the longitudinal storage modulus M', where M_0 is the low frequency modulus. Figure 8 shows a comparison between the resulting longitudinal relaxation times, λ_{long}, and those obtained from experiment using a (i) Debye model [3], (ii) linewidth analysis [45,46], and (iii) mode-coupling theory [47]. Experimental and simulation data are of similar magnitude across the temperature spectrum, but experiment displays a stronger decrease in relaxation time with temperature.

C. Generalized Cauchy relationship

Figure 9 shows that a generalized Cauchy relationship (gCR) with $M_\infty = 3.07\,G_\infty + 4.21$ (GPa) holds for SPC/E water ($R^2 = 0.925$), where we have again assumed $G_\infty \approx G'_{2\,\text{THz}}$ and $M_\infty \approx M'_{2\,\text{THz}}$. A gCR is obeyed by isotropic crystals and solids whose atoms predominantly interact through a central potential. It is predicted that viscoelastic liquids will also obey a gCR [48], which is supported by the gCR of the SPC/E model for water. Additionally, this observed gCR suggests that the driving mechanism for the elastic response of the SPC/E model is dominated by central
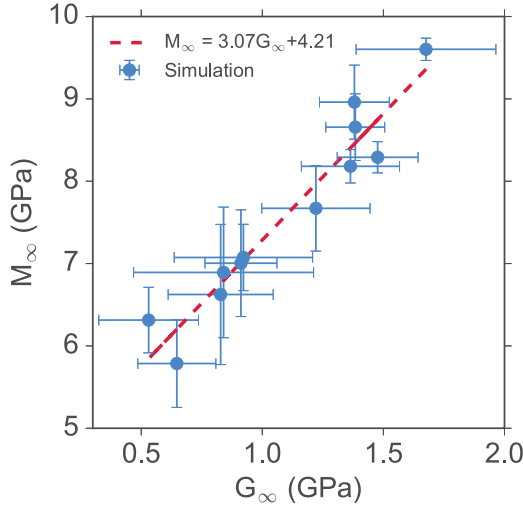
FIG. 9. Simulation data for the high frequency longitudinal modulus, M_∞, versus the corresponding shear modulus, G_∞, of the SPC/E model of water; the data provided are for a frequency of $f = 2$ THz. Also shown is a comparison of simulation data to a gCR fit. The error bars represent one standard deviation.

forces. Furthermore, it should be noted that the gCR for the SPC/E model is strikingly similar to that found for the glycerol model from the same simulation method [25], where it was previously found that $M_\infty^{\mathrm{glycerol}} = 2.98\, G_\infty^{\mathrm{glycerol}} + 4.50$ (GPa).

D. Time temperature superposition

Finally, we apply the time temperature superposition principle [49] to the SPC/E model data for both the shear and compressional moduli. This involves determining the frequency multiplicative factor, a_T, as a function of temperature, T, that collapses the simulated data at a chosen temperature, T, to that at fixed reference temperature, T_0, i.e.,

$$X(f, T) = X(a_T f, T_0), \tag{20}$$

where the symbol, X, represents any one of the (storage or loss) shear or compressional moduli, which depend on both frequency, f, and temperature, T. In polymer rheology, T_0 is often chosen to be the glass transition temperature. Because we study SPC/E water in its liquid phase near standard temperature and pressure, we instead choose $T_0 = 293$ K as a nominal value; the SPC/E dataset is generated well above the glass transition temperature for water. Simulated data in the frequency range 50–2000 GHz are used.

Figures 10(a) and 10(b) show master curves for the shear and compressional moduli (storage and loss) using only the storage shear modulus, G', at $T_0 = 293$ K as reference to determine a_T; this uses $T = 273, 283, 298, 303, 313, 323, 333, 343, 353, 363, 373$ K, a subset of which is given in Fig. 2. The extracted a_T versus T relationship which is applied to generate Figs. 10(a) and 10(b) is given in Fig. 10(c), and is well approximated by the empirical fit function,

$$\log_{10} a_T = -2.68 \left(\frac{T}{293} - 1 \right) + 0.942 \left(\frac{T}{293} - 1 \right)^2. \tag{21}$$

It decreases monotonically with increasing temperature, as expected [49]. We refrain from using the Williams-Landel-Ferry (WLF) model [49] because the dataset is well above its glass transition temperature.
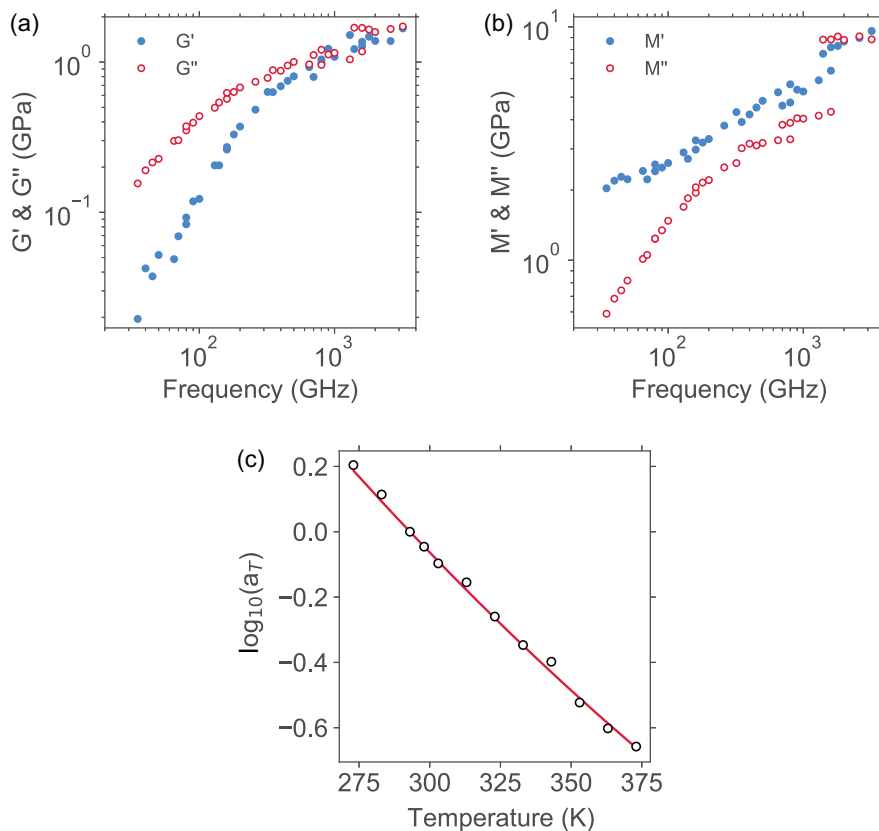
FIG. 10. Application of the time temperature superposition principle to simulation data for (a) shear moduli, G' and G'', (b) compressional moduli, M' and M''. The extracted a_T versus T relation (dots), using the dataset for G' at $T_0 = 293$ K is shown in (c), along with the fit curve in Eq. (21).

Strikingly, the time temperature superposition principle is well satisfied in Figs. 10(a) and 10(b) with moduli data in Fig. 2 (and at the intermediate temperatures listed above) collapsing, even though the a_T versus T relationship is determined using the G' dataset alone. As expected, the time temperature superposition principle generates moduli data outside of the frequency range for which the moduli are simulated; see data with frequencies below 50 GHz in Figs. 10(a) and 10(b) that arise because values with $a_T < 1$ exist [Fig. 10(c)].

An anomaly is observed in Figs. 10(a) and 10(b) at the highest frequencies (>1.5 THz), particularly in M'' where a plateau is clear—this plateau comes from simulated data at 2 THz alone, which is the threshold discussed in the previous sections. This suggests that the time temperature superposition principle does not apply in the high frequency range (>2 THz), pointing towards different physics to that observed at lower frequencies. Examination of the mechanisms underlying the viscoelasticity of water in this high frequency range presents an interesting avenue for future work.

IV. CONCLUSIONS

This study demonstrates that a previously reported nonequilibrium molecular dynamics methodology [25] for determining the viscoelastic properties of glycerol can be successfully applied to water (and many other simple liquids). This methodology and equilibrium simulations involving the Green-Kubo relations [22–24] were used to simulate a viscoelastic dataset of the SPC/E model for

water across its liquid phase and for frequencies up to and including 10 THz. These two independent simulation approaches gave identical results.

Data up to and including 2 THz was fitted to a single relaxation time Maxwell model, enabling comparison to available experimental measurements. The associated relaxation times of the Maxwell model fits were described empirically by Eqs. (18a) and (18b). These relaxation times were found to be in agreement with existing measurements of shear while a significant discrepancy was observed for the compressional relaxation times.

It was shown that the SPC/E model satisfies a gCR suggesting that its viscoelastic behavior may be simplified through the use of central potentials. Both elastic and loss moduli obey the time temperature superposition principle for frequencies below 2 THz only. This points to different physics above this frequency range, whose exploration provides an avenue for future work.

APPENDIX A: STRAIN AMPLITUDES AND SIMULATION DETAILS

To ensure the viscoelastic response of the simulation samples is linear, the strain-amplitudes γ_0 and ε_0 in Eq. (1) must be chosen appropriately. Three methods are used to select these parameters, each requiring a strain-amplitude sweep at fixed temperature.

First, plots of stress versus strain-rate for a linear viscoelastic material must form an ellipse, provided the data is sufficiently noise-free. Such plots are commonly referred to as "Lissajous loops." Second, all viscoelastic moduli must be independent of strain-amplitude when the viscoelastic response is linear. Thus, the values of γ_0 and ε_0 in Eq. (1) should be chosen from the subset of strains in the strain-sweep which do not significantly affect the value of the viscoelastic moduli. Finally, a linear viscoelastic response must manifest itself as a single peak in the discrete Fourier transform (DFT) of the stress time series. Thus, acceptable choices for γ_0 and ε_0 are those that do not give rise to additional harmonics in the DFT. In this Appendix, a strain-sweep is performed for a frequency of $f = 500\,\text{GHz}$ and temperature of $T = 298\,\text{K}$.

By applying the three methods mentioned above, it is found that the choice of $\gamma_0 = \varepsilon_0 = d/L_x = 0.0075$ maximizes the signal-to-noise while maintaining linearity, where d is the displacement of the box and L_x is the side length in the x-direction. Examples of the Lissajous loops highlighting this linearity are shown in Fig. 11.

A temperature sweep is then performed for $f = 500\,\text{GHz}$ and $\gamma_0 = \varepsilon_0 = 0.0075$ to ensure that the response is linear across all temperatures of interest. Hence, $\gamma_0 = \varepsilon_0 = 0.0075$ guarantees a linear viscoelastic response for all simulations where $f \leqslant 500\,\text{GHz}$. This process is then repeated for $f = 5, 10$ THz. It is found that the choices of $\gamma_0 = \varepsilon_0 = 0.0015, 0.00055$ proves optimal. Hence, our strain amplitudes are as follows:

$$\gamma_0 = \varepsilon_0 = \begin{cases} 0.0075, & f \leqslant 0.5\,\text{THz}, \\ 0.0015, & 0.5\,\text{THz} < f \leqslant 5\,\text{THz}, \\ 0.00055, & 5\,\text{THz} < f \leqslant 10\,\text{THz}. \end{cases} \tag{A1}$$

The simulation duration is two million time-steps. To ensure that the number of simulation time-steps per oscillation time period is reasonably consistent across all frequencies, the time-step (fs)
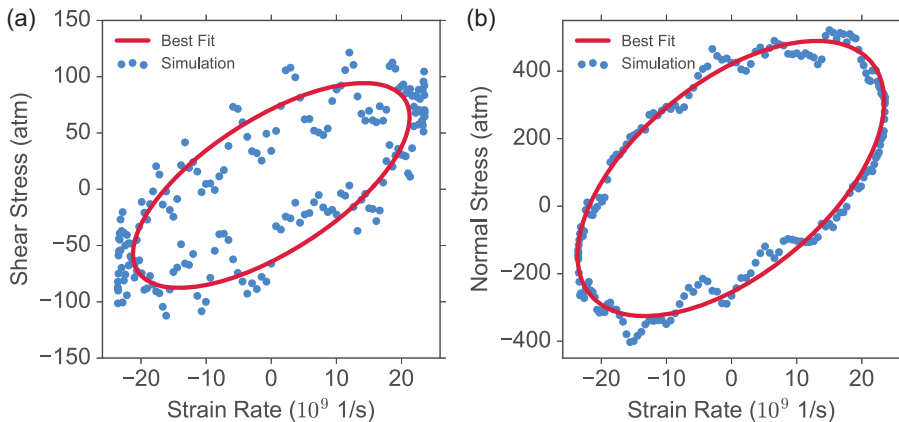
FIG. 11. Lissajous loops obtained from simulation data. (a) Shear and (b) elongation with $\gamma_0 = 0.0075$, $f = 500\,\text{GHz}$, $T = 298\,\text{K}$. Both sets of data are well fit to ellipses showing that a strain-amplitude of $\gamma_0 = 0.0075$ gives a linear-viscoelastic response for both shear and elongation.

varies as the following function of frequency, f:

$$\Delta t = \begin{cases} 1.0, & f \leqslant 0.2\,\text{THz}, \\ 0.1, & 0.2\,\text{THz} < f \leqslant 2\,\text{THz}, \\ 0.01, & 2\,\text{THz} < f \leqslant 10\,\text{THz}. \end{cases} \tag{A2}$$

APPENDIX B: ATOMIC PRESSURE TENSOR AND SLLOD

We justify use of the atomic thermostat, atomic pressure tensor and atomic SLLOD with reference to the Weissenberg number, Wi, defined as the ratio of elastic forces to viscous forces in the material. For shear and elongation, the associated Weissenberg numbers are

$$\text{Wi}_{\text{sh}} = 2\pi f \gamma_0 \lambda_{\text{sh}}, \quad \text{Wi}_{\text{long}} = 2\pi f \varepsilon_0 \lambda_{\text{long}}, \tag{B1}$$

where λ_{sh} and λ_{long} are the shear and longitudinal relaxation times of material, respectively.

When the Weissenberg number approaches $\text{Wi} = 1$, the linear response of the fluid can no longer be sampled. Furthermore, the use of an atomic thermostat, stress-tensor and SLLOD algorithm (as implemented by LAMMPS), as opposed to their molecular counterparts, may be invalid. This is because it is known that an incorrectly formulated atomic thermostat used in conjunction with the atomic SLLOD algorithm will fail to account for rotational degrees of freedom, resulting in incorrect stresses and artificially enhanced alignment of the molecules (see Ref. [36] and references therein). While this is a serious problem for Weissenberg numbers approaching 1, it can be reasonably ignored for small Weissenberg numbers, where the atomic and molecular approaches will be approximately equivalent. In our simulations, the largest Wi_{sh} and Wi_{long} to be reached are

$$\text{Wi}_{\text{sh}} = 0.050, \quad \text{Wi}_{\text{long}} = 0.065. \tag{B2}$$

These values are obtained from the largest strain-rates used in our simulations and the longest relaxation times derived from experiments [2,3]. Given these values are two orders of magnitude less than 1, this observation indicates that our simulations are approximately equivalent to those performed using a molecular thermostat, stress-tensor and SLLOD algorithm.

APPENDIX C: COMPLETE VISCOELASTIC DATASET

All viscoelastic data obtained for the SPC/E model of water are given in Tables I–IV.

TABLE I. Storage modulus, G' (GPa), versus frequency, f (GHz), and temperature, T (K).

T (K)	50	100	200	500	1000	2000	5000	10 000
	f (GHz)							
273	0.08318	0.2718	0.6328	1.041	1.28	1.676	−0.2185	9.538
283	0.04878	0.2054	0.4822	0.9262	1.515	1.38	0.1588	9.556
293	0.05201	0.1228	0.3722	0.8042	1.084	1.384	1.131	9.819
298	0.03749	0.1183	0.3296	0.7503	1.226	1.476	0.6372	10.14
303	0.04234	0.09228	0.2619	0.6909	0.9904	1.364	1.017	9.91
313	0.01952	0.06927	0.2055	0.6309	0.7966	1.221	0.4607	8.474
323	0.003115	0.05037	0.1513	0.5035	0.841	0.9219	1.326	8.254
333	0.01015	0.0295	0.1038	0.434	0.889	0.8401	1.127	8.296
343	0.01088	0.01803	0.1086	0.4003	0.6206	0.9117	0.6089	8.809
353	0.00262	0.002997	0.07491	0.2592	0.6425	0.828	0.5102	5.821
363	0.006264	−0.0009899	0.05005	0.2879	0.5625	0.5307	0.2486	6.615
373	0.006022	0.01178	0.04656	0.2807	0.4252	0.647	1.167	6.547

TABLE II. Loss modulus, G'' (GPa), versus frequency, f (GHz), and temperature, T (K).

T (K)	50	100	200	500	1000	2000	5000	10 000
	f (GHz)							
273	0.3511	0.5688	0.7845	0.9583	1.177	1.727	5.139	5.386
283	0.2988	0.4967	0.7393	0.9657	1.042	1.66	5.375	7.479
293	0.2271	0.4367	0.678	1.003	1.151	1.586	4.462	5.785
298	0.2149	0.395	0.6324	0.9483	1.124	1.648	4.664	7.049
303	0.1903	0.3735	0.6243	0.8751	1.208	1.689	4.995	6.356
313	0.1556	0.302	0.5385	0.8835	1.114	1.695	4.413	7.1
323	0.1396	0.3104	0.5026	0.9444	1.298	1.698	4.86	6.398
333	0.1307	0.2491	0.4592	0.858	1.022	1.655	5.255	5.03
343	0.09687	0.2291	0.4267	0.8003	1.178	1.597	4.656	6.697
353	0.107	0.2062	0.3871	0.7432	1.218	1.631	4.642	6.228
363	0.09754	0.1908	0.3507	0.7585	1.369	1.619	4.768	6.378
373	0.06716	0.1774	0.3167	0.7076	1.25	1.614	4.857	6.752

TABLE III. Storage modulus, M' (GPa), versus frequency, f (GHz), and temperature, T (K).

	f (GHz)							
T (K)	50	100	200	500	1000	2000	5000	10 000
273	2.572	3.261	4.311	5.672	6.49	9.602	13.16	25.4
283	2.412	2.896	3.773	5.246	5.905	8.961	11.97	23.92
293	2.224	2.609	3.307	4.819	5.286	8.657	12.22	25.35
298	2.278	2.494	3.192	4.512	5.379	8.291	11.63	25.5
303	2.191	2.406	2.976	4.213	4.741	8.181	12.4	23.78
313	2.033	2.22	2.72	3.911	4.597	7.671	11.19	22.57
323	2.01	2.125	2.473	3.508	4.352	7.074	11.1	23.23
333	1.863	1.996	2.256	3.123	3.907	6.893	10.78	23.35
343	1.84	1.861	2.079	2.815	3.626	7.004	10.38	23.24
353	1.728	1.762	1.947	2.679	3.162	6.624	10.22	20.48
363	1.722	1.743	1.865	2.372	3.026	6.314	11.14	21.7
373	1.579	1.569	1.705	2.149	2.586	5.786	10.73	18.84

TABLE IV. Loss modulus, M'' (GPa), versus frequency, f (GHz), and temperature, T (K).

	f (GHz)							
T (K)	50	100	200	500	1000	2000	5000	10 000
273	1.237	1.946	2.608	3.297	4.326	8.837	11.25	10.71
283	1.012	1.693	2.499	3.266	4.163	9.113	10.69	10.24
293	0.8176	1.475	2.204	3.179	4.042	8.801	10.97	10.75
298	0.742	1.342	2.151	3.102	4.058	9.1	11.43	10.6
303	0.684	1.236	2.053	3.157	3.879	8.834	11.19	12.68
313	0.5891	1.053	1.842	3.02	3.806	8.821	11.13	10.93
323	0.4852	0.9441	1.712	2.992	4.368	8.897	10.95	11.44
333	0.4268	0.834	1.525	2.846	4.192	8.917	11.2	10.77
343	0.354	0.7593	1.393	2.649	3.807	8.652	10.93	8.437
353	0.3656	0.6556	1.261	2.493	4.294	8.387	10.82	10.13
363	0.3169	0.6178	1.198	2.407	3.867	8.662	10.64	9.303
373	0.2794	0.5819	1.115	2.245	3.556	8.418	9.696	9.163
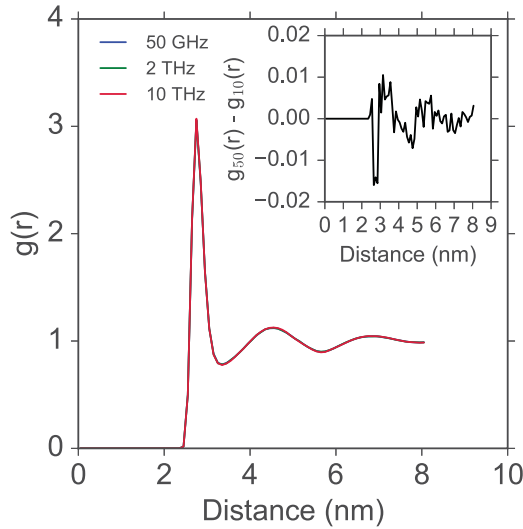
FIG. 12. Oxygen-oxygen pair distribution functions for frequencies $f = 50$ GHz, 2 THz, and 10 THz at a temperature of $T = 298$ K. The inset is the difference between the O-O PDF at 50 GHz and 10 THz.

APPENDIX D: OXYGEN-OXYGEN PAIR DISTRIBUTION FUNCTION

Figure 12 shows the oxygen-oxygen pair distribution functions (O-O PDF) for SPC/E water calculated from three shear simulations at a temperature of 298 K and frequencies of 50 GHz, 2 THz, and 10 THz. The O-O PDFs for each frequency cannot be distinguished by eye, thus the difference between the 50 GHz O-O PDF and the 10 THz O-O PDF is plotted in the inset of Fig. 12. The difference is two orders of magnitude smaller than the original O-O PDFs, suggesting that no structural changes occur as frequency increases. This confirms there is no transition into the string phase suggested in Sec. III. Note that we only need to investigate the O-O PDFs for shear as the artificial alignment associated with the string phase only occurs due to an incorrect assumption of a profile biased thermostat (discussed above). Elongational flow does not excite the rotational degrees of freedom of the molecules, hence should not suffer from such assumptions.

[1] R. Piccirelli and T. A. Litovitz, Ultrasonic shear and compressional relaxation in liquid glycerol, J. Acoust. Soc. Am. **29**, 1009 (1957).

[2] W. M. Slie, A. R. Donfor Jr., and T. A. Litovitz, Ultrasonic shear and longitudinal measurements in aqueous glycerol, J. Chem. Phys. **44**, 3712 (1966).

[3] A. Cunsolo, G. Ruocco, F. Sette, C. Masciovecchio, A. Mermet, G. Monaco, M. Sampoli, and R. Verbeni, Experimental Determination of the Structural Relaxation in Liquid Water, Phys. Rev. Lett. **82**, 775 (1999).

[4] G. Monaco, A. Cunsolo, G. Ruocco, and F. Sette, Viscoelastic behavior of water in the terahertz-frequency range: An inelastic x-ray scattering study, Phys. Rev. E **60**, 5505 (1999).

[5] C. Masciovecchio, S. C. Santucci, A. Gessini, S. Di Fonzo, G. Ruocco, and F. Sette, Structural Relaxation in Liquid Water by Inelastic UV Scattering, Phys. Rev. Lett. **92**, 255507 (2004).

[6] A. Giugni and A. Cunsolo, Structural relaxation in the dynamics of glycerol: A joint visible, UV and x-ray inelastic scattering study, J. Phys.: Condens. Matter **18**, 889 (2006).

[7] Y. H. Jeong, S. R. Nagel, and S. Bhattacharya, Ultrasonic investigation of the glass transition in glycerol, Phys. Rev. A **34**, 602 (1986).

 [8] Y. H. Jeong, Frequency-dependent shear modulus of glycerol near the glass transition, Phys. Rev. A **36**, 766 (1987).

 [9] R. H. Cole and D. W. Davidson, High frequency dispersion in *n*-propanol, J. Chem. Phys. **20**, 1389 (1952).

[10] C. Klieber, T. Hecksher, T. Pezeril, D. H. Torchinsky, J. C. Dyre, and K. A. Nelson, Mechanical spectra of glass-forming liquids. II. Gigahertz-frequency longitudinal and shear acoustic dynamics in glycerol and DC704 studied by time-domain Brillouin scattering, J. Chem. Phys. **138**, 12A544 (2013).

[11] M. Pelton, D. Chakraborty, E. Malachosky, P. Guyot-Sionnest, and J. E. Sader, Viscoelastic Flows in Simple Liquids Generated by Vibrating Nanostructures, Phys. Rev. Lett. **111**, 244502 (2013).

[12] K. Yu, T. A. Major, D. Chakraborty, M. S. Devadas, J. E. Sader, and G. V. Hartland, Compressible viscoelastic liquid effects generated by the breathing modes of isolated metal nanowires, Nano Lett. **15**, 3964 (2015).

[13] V. Juvé, A. Crut, P. Maioli, M. Pellarin, M. Broyer, N. Del Fatti, and F. Vallée, Probing elasticity at the nanoscale: Terahertz acoustic vibration of small metal nanoparticles, Nano Lett. **10**, 1853 (2010).

[14] J. P. Wittmer, H. Xu, P. Polińska, F. Weysser, and J. Baschnagel, Shear modulus of simulated glass-forming model systems: Effects of boundary condition, temperature, and sampling time, J. Chem. Phys. **138**, 12A533 (2013).

[15] P. S. Stephanou and V. G. Mavrantzas, Accurate prediction of the linear viscoelastic properties of highly entangled mono and bidisperse polymer melts, J. Chem. Phys. **140**, 214903 (2014).

[16] M. Vladkov and J.-L. Barrat, Linear and nonlinear viscoelasticity of a model unentangled polymer melt: Molecular dynamics and Rouse modes analysis, Macromol. Theory Simul. **15**, 252 (2006).

[17] H.-C. Tseng, J.-S. Wu, and R.-Y. Chang, Linear viscoelasticity and thermorheological simplicity of *n*-hexadecane fluids under oscillatory shear via nonequilibrium molecular dynamics simulations, Phys. Chem. Chem. Phys. **12**, 4051 (2010).

[18] C.-C. Wang and R.-Y. Chang, Nonlinearity and slip behavior of *n*-hexadecane in large amplitude oscillatory shear flow via nonequilibrium molecular dynamic simulation, J. Chem. Phys. **136**, 104904 (2012).

[19] A. Rahman and F. H. Stillinger, Propagation of sound in water. A molecular-dynamics study, Phys. Rev. A **10**, 368 (1974).

[20] F. Sciortino and S. Sastry, Sound propagation in liquid water: The puzzle continues, J. Chem. Phys. **100**, 3881 (1994).

[21] U. Balucani, G. Ruocco, A. Torcini, and R. Vallauri, Fast sound in liquid water, Phys. Rev. E **47**, 1677 (1993).

[22] M. S. Green, Markoff random processes and the statistical mechanics of time-dependent phenomena. II. irreversible processes in fluids, J. Chem. Phys. **22**, 398 (1954).

[23] R. Kubo, Statistical-mechanical theory of irreversible processes. I. general theory and simple applications to magnetic and conduction problems, J. Phys. Soc. Jpn. **12**, 570 (1957).

[24] R. Zwanzig and R. D. Mountain, High-frequency elastic moduli of simple fluids, J. Chem. Phys. **43**, 4464 (1965).

[25] N. M. Lacevic and J. E. Sader, Viscoelasticity of glycerol at ultra-high frequencies investigated via molecular dynamics simulations, J. Chem. Phys. **144**, 054502 (2016).

[26] Y. Wu, H. L. Tepper, and G. A. Voth, Flexible simple point-charge water model with improved liquid-state properties, J. Chem. Phys. **124**, 024503 (2006).

[27] N.-S. Cheng, Formula for the viscosity of a glycerol-water mixture, Ind. Eng. Chem. Res. **47**, 3285 (2008).

[28] M. J. Holmes, N. G. Parker, and M. J. W. Povey, Temperature dependence of bulk viscosity in water using acoustic spectroscopy, J. Phys.: Conf. Ser. **269**, 012011 (2011).

[29] H. J. C. Berendsen, J. R. Grigera, and T. P. Straatsma, The missing term in effective pair potentials, J. Phys. Chem. **91**, 6269 (1987).

[30] L. Martínez, R. Andrade, E. G. Birgin, and J. M. Martínez, PACKMOL: A package for building initial configurations for molecular dynamics simulations, J. Comput. Chem. **30**, 2157 (2009).

[31] S. Plimpton, Fast parallel algorithms for short-range molecular dynamics, J. Comput. Phys. **117**, 1 (1995).

[32] W. Shinoda, M. Shiga, and M. Mikami, Rapid estimation of elastic constants by molecular dynamics simulation under constant stress, Phys. Rev. B **69**, 134103 (2004).

[33] M. Parrinello and A. Rahman, Polymorphic transitions in single crystals: A new molecular dynamics method, J. Appl. Phys. **52**, 7182 (1981).

[34] G. J. Martyna, D. J. Tobias, and M. L. Klein, Constant pressure molecular dynamics algorithms, J. Chem. Phys. **101**, 4177 (1994).

[35] D. J. Morris and G. P. Morriss, *Statistical Mechanics of Nonequilibrium Liquids* (Academic Press, London, 1990).

[36] B. D. Todd and P. J. Daivis, *Nonequilibrium Molecular Dynamics: Theory, Algorithms and Applications* (Cambridge University Press, Cambridge, UK, 2017).

[37] P. J. Daivis and B. D. Todd, A simple, direct derivation and proof of the validity of the sllod equations of motion for generalized homogeneous flows, J. Chem. Phys. **124**, 194103 (2006).

[38] D. J. Evans and G. P. Morriss, Non-newtonian molecular dynamics, Comput. Phys. Rep. **1**, 297 (1984).

[39] M. H. Nafar Sefiddashti, B. J. Edwards, and B. Khomami, Individual chain dynamics of a polyethylene melt undergoing steady shear flow, J. Rheol. **59**, 119 (2015).

[40] M. H. Nafar Sefiddashti, B. J. Edwards, and B. Khomami, Individual molecular dynamics of an entangled polyethylene melt undergoing steady shear flow: Steady-state and transient dynamics, Polymers **11**, 476 (2019).

[41] B. J. Edwards and M. Dressler, A reversible problem in nonequilibrium thermodynamics: Hamiltonian evolution equations for nonequilibrium molecular dynamics simulations, J. Non-Newtonian Fluid Mech. **96**, 163 (2001).

[42] M. E. Tuckerman, C. J. Mundy, S. Balasubramanian, and M. L. Klein, Modified nonequilibrium molecular dynamics for fluid flows with energy conservation, J. Chem. Phys. **106**, 5615 (1997).

[43] Personal communication, 4 September 2019, Pieter J. in 't Veld (pieter.intveld@basf.com), original programmer of SLLOD code in LAMMPS.

[44] G. S. Fanourgakis, J. S. Medina, and R. Prosmiti, Determining the bulk viscosity of rigid water models, J. Phys. Chem. A **116**, 2564 (2012).

[45] V. Mazzacurati, A. Nucara, M. A. Ricci, G. Ruocco, and G. Signorelli, High-resolution low-frequency raman spectra of liquid H_2O and D_2O, J. Chem. Phys. **93**, 7767 (1990).

[46] A. Fontana, M. Nardone, and M. A. Ricci, Depolarized rayleigh scattering in water up to supercritical conditions, J. Chem. Phys. **102**, 6975 (1995).

[47] A. P. Sokolov, J. Hurst, and D. Quitmann, Dynamics of supercooled water: Mode-coupling theory approach, Phys. Rev. B **51**, 12865 (1995).

[48] D. Fioretto, S. Corezzi, S. Caponi, F. Scarponi, G. Monaco, A. Fontana, and L. Palmieri, Cauchy relation in relaxing liquids, J. Chem. Phys. **128**, 214502 (2008).

[49] R. M. Christensen, *Theory of Viscoelasticity: An Introduction* (Academic Press, New York, 1982).